PLASMA PROCESSES
AND POLYMERS

Large-area atmospheric pressure dielectric barrier discharges in Ar–HMDSO mixtures: Experiments and fluid modelling

Detlef Loffhagen[1] | **Markus M. Becker[1]** | **Dirk Hegemann[2]** | **Bernard Nisol[3]** | **Sean Watson[3]** | **Michael R. Wertheimer[3]** | **Claus-Peter Klages[4]**

[1]Leibniz Institute for Plasma Science and Technology (INP), Greifswald, Germany

[2]Empa, Swiss Federal Laboratories for Materials Science and Technology, Plasma and Coating Group, St. Gallen, Switzerland

[3]Groupe des Couches Minces (GCM), Department of Engineering Physics, Polytechnique Montréal, Montréal, Quebec, Canada

[4]Institute for Surface Technology, TU Braunschweig, Braunschweig, Germany

Correspondence
Detlef Loffhagen, Leibniz Institute for Plasma Science and Technology (INP), Felix-Hausdorff-Str. 2, 17489 Greifswald, Germany.
Email: loffhagen@inp-greifswald.de

Abstract

The electrical discharge characteristics of a large-area experimental dielectric barrier discharge in argon–hexamethyldisiloxane mixtures containing up to about 1,600 ppm of the monomer is analysed by means of electrical measurements and numerical modelling. A time-dependent, spatially one-dimensional fluid model is employed, taking into account the spatial variation of the discharge plasma between the two plane-parallel dielectrics covering the electrodes. Reasonable agreement between electrical measurements and modelling results is generally found for the gap voltages and discharge currents. Remaining differences between the measured and calculated electrical energy dissipated in the plasma per period are discussed.

KEYWORDS

dielectric barrier discharge, HMDSO, modelling, plasma polymerisation
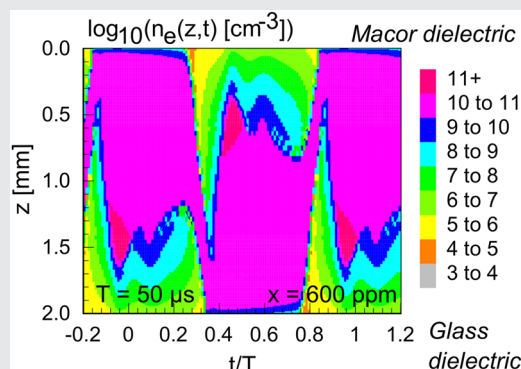
1 | INTRODUCTION

Hexamethyldisiloxane (HMDSO) has been used as a prototype precursor (so-called monomer) for the plasma deposition of organosilicon thin films for several decades. It is a volatile, colourless liquid with a vapour pressure of 55 mbar at room temperature of 298 K.[1] It is nonflammable, comparatively nontoxic, and cheap.[2]

Although earlier literature mostly dealt with the film deposition from pure HMDSO or HMDSO mixed with different carrier gases using low-pressure nonthermal plasmas,[3–19] there has been growing interest in its plasma polymerisation at atmospheric pressure more

recently. In addition to atmospheric pressure plasma jets,[20–25] which have been developed for a localised deposition of organosilicon thin films, dielectric barrier discharges (DBDs) have mostly been employed as a source for plasma-enhanced chemical vapour deposition processes.[26–36] Here, only small amounts of HMDSO are admixed to a carrier gas like helium, argon, nitrogen, or air for the deposition of HMDSO-based plasma polymer films at ambient pressure. In contrast to thermal CVD processes, these carrier gases are not just diluents, but they play a very important role in the mechanism of plasma-activated film deposition at atmospheric pressure. Although monomer fractions, x, of 5.5% (55,000 ppm) can

be achieved by saturation of the gas phase with HMDSO at 298 K and 1 bar, maximum mole fractions of only a few thousand ppm or even much less have mostly been applied to obtain smooth and particle-free films of plasma-polymerised HMDSO (pp-HMDSO).

At such strong degrees of dilution in Ar or He, the excitation, dissociation, and ionisation of monomer molecules by direct electron collisions play a negligible role, when compared with corresponding processes driven by excited noble gas atoms or noble gas ions, transferring energy or charge to a monomer molecule, as shown in a recently published numerical study.[37] Here, DBDs in argon with small admixtures, $x \leq 300$ ppm, of HMDSO were analysed using a time-dependent, spatially one-dimensional fluid-Poisson model. A comparison of the results of model calculations with experimental data faces a dilemma. On the one hand, to approximate electrical one-dimensionality in the experiment, the electrode dimensions perpendicular to the electric field should be made much larger than the widths of the gas gap and dielectrics, so as to render edge effects negligibly small. On the other hand, increasing the length of the electrodes, that is, their extension in the gas flow direction, inevitably enhances chemical inhomogeneities due to plasma-chemical conversion, along with film deposition during the passage of the monomer through the plasma zone. For these reasons, a plane-parallel discharge configuration with rectangular electrodes having a length of only 1 cm in the gas flow direction, a width of 8 cm, and a discharge gap of 1 mm had been investigated in the previous experiments.[36,37]

On the basis of an established reaction kinetics scheme for argon,[38] which was extended by 21 collision processes of HMDSO ((CH_3)$_3$SiOSi(CH_3)$_3$) with electrons, different excited states of argon atoms and molecules, and atomic and molecular argon ions, as well as the dissociative recombination of electrons due to collisions with the pentamethyldisiloxanyl ion (CH_3)$_3$SiOSi$^+$(CH_3)$_2$, the fluid model calculations were able to reproduce several discharge characteristics reasonably well. This concerns, for instance, the temporal evolution of the discharge current for the DBD experiments in an Ar–HMDSO mixture with 300 ppm HMDSO reported by Morent et al.[30] as well as the measured substantial decrease of the ignition voltage and the dissipated power at a constant applied voltage with growing x.[36,37] Penning ionisation processes due to energy transfer from excited (metastable and resonance) argon atoms to HMDSO were found to become the predominant source for the production of electrons above about $x = 5$ ppm in the small-scale DBD reactor. Furthermore, it turned out that the production of the neutral trimethylsilyl ((CH_3)$_3$Si) and trimethylsiloxy ((CH_3)$_3$SiO) radicals,

which are the main precursors of the deposited film,[39,40] also takes place largely due to the collision of HMDSO with excited argon atoms and molecules, followed by dissociation.

A drawback of the small-scale electrode configuration with a length of only 1 cm in the gas flow direction is its relatively large effect of electrode edges and the resulting fringing electric fields, rendering difficult a direct comparison of the temporal behaviour of electrical discharge properties for operating conditions typical of deposition experiments.[37] For example, an experimental value of 6.6 pF was obtained for the cell capacitance,[36] a factor of 1.74 larger than that calculated using the equation for an ideal parallel-plate capacitor (3.79 pF).

For this reason, the experimental results obtained in a significantly larger DBD reactor are of greater interest for benchmarking the model calculations. Experimental data from experiments using the DBD reactor described by Nisol et al.,[41] which was also applied to studies using HMDSO as a precursor,[33,35] are of particular interest here, as much effort has been invested in its precise electrical characterisation and process monitoring. Therefore, the results of the corresponding comparative experimental and modelling studies are presented and discussed in the current paper, where the same numerical model as in Loffhagen et al.[37] has been employed for the model calculations. The range of HMDSO fractions (x) studied extends up to 1,600 ppm, in accordance with an experimental work,[33] instead of only 300 ppm as in the previous paper.

In addition to the comparison of voltages and currents obtained by experiments and modelling, a detailed discussion of the ionisation budget and the energy loss due to HMDSO is performed. Certain differences related to the dependence of the measured and calculated electrical energy dissipated in the discharge per period on the initial monomer fraction are comprehensively discussed. This concerns, in particular, the possibility of nanoparticle formation and the depletion of HMDSO, which can become important in large-area reactors with longer residence times.

2 | EXPERIMENTAL SECTION

The construction of the large-area DBD reactor used for plasma polymerisation experiments is described in detail by Nisol et al.[41] and corresponding studies for a 10 slm (standard liters per minute) flow of argon doped with a monomer gas flow, F_m, of HMDSO up to about 16 sccm, that is, $x = 1,600$ ppm, are reported in the literature.[33,35] Figure 1 shows a schematic representation of this DBD reactor. It consists of two polished aluminum electrodes

FIGURE 1 Schematic representation of the dielectric barrier discharge reactor used for plasma polymerisation experiments. HV, high-voltage; LV, low-voltage

FIGURE 2 Equivalent electrical circuit of the experimental set-up, where the portion in the dashed rectangle represents the dielectric barrier discharge cell. The values of the equivalent circuit model elements C_1, C_2, C_{die}, C_{gap}, R, and R_m are given in the literature[43,44]

(A), each $18\,cm \times 6\,cm \times 1.75\,mm$ in size and connected to a high-voltage (HV) power supply, the top dielectric barrier (M) made of Macor with a thickness $\Delta_M = 3.5\,mm$ and relative permittivity $\varepsilon_r = 6.0$, the bottom dielectric barrier (G) made of glass ($\Delta_G = 3.0\,mm$ and $\varepsilon_r = 4.0$), and a moveable grounded electrode plate (E). The discharge gap between the two dielectrics is $d = 2\,mm$. From these data, the discharge area and volume can be evaluated at $A = 216\,cm^2$ and $V = 43.2\,cm^3$, respectively. The feed gas injector (F) is also made of Macor and is 24 cm x 3 cm x 1.27 cm in size. It is provided with channels with a diameter of 6.35 mm to allow gas injection from the top as well as from the sides. On the bottom, 22 holes (3 mm in diameter) permit a homogeneous distribution of feed gas across the entire width of a moving or static substrate.

The HV power supply comprises an AC generator (Hewlett-Packard 3310A), a power amplifier (Model RMX2450; QSC Ltd.), and an HV transformer (Model LM2727-03; Enercon). The AC power supply voltage $V_{ps}(t)$ with a typical frequency $f = 20$ kHz used in the experimental studies[33] is monitored by means of an HV probe (P6015A; Tektronix). The lower electrode (E) is connected to the ground via the $50\,\Omega$ precision resistor R_m, which serves to measure the voltage signal V_m by means of a low-voltage (LV) probe and, thus, to determine the measured current $I_m = V_m/R_m$. The voltage and current signals are synchronously displayed using a digital storage oscilloscope (200 MHz, GDS-2204A; Instek). These data are transmitted and acquired in real-time by means of a USB (universal serial bus) link on a PC, where they are postprocessed.

The equivalent electrical circuit model for the entire experimental set-up is displayed in Figure 2. Here, the portion inside the dashed rectangle corresponds to the discharge cell itself and Z_d is a nonlinear variable impedance. Its value is not known with precision, but it

tends towards zero during discharges and towards infinity between discharges. By applying Kirchhoff's laws to this equivalent circuit, a set of equations results, which allows one to calculate the voltage across the discharge gap, V_{gap}, the displacement current in the gap, I_{gap}, the discharge current I_d, representing the conduction current in the gap, and the gas current I_g. The electrical energy E_g dissipated in the gas discharge per period, $T = 1/f$, is derived in the experimental analysis according to

$$E_g = \int_{t_0}^{t_0+T} I_d(t) V_{gap}(t)\,dt \qquad (1)$$

using the measured voltage signals $V_{ps}(t)$ and $V_m(t)$.[33] The details of the methodology are given by Archambault-Caron et al.[42] and corrected values of the elements of the equivalent circuit model are reported in recent literature.[43,44]

Figure 3 illustrates the measured dependence of E_g on F_m for an argon flow of 10 slm at an applied AC voltage $V_a(t)$ with an amplitude $V_{a,0} = 3.9$ kV and a frequency $f = 20$ kHz. At these conditions, the residence time of the gas mixture in the plasma zone amounts to about

FIGURE 3 Measured energy E_g dissipated in the discharge per period and its change ΔE_g upon addition of HMDSO as a function of the monomer gas flow F_m in 10 slm Ar at an applied voltage amplitude $V_{a,0} = 3.9$ kV and $f = 20$ kHz

260 ms.[41] Furthermore, the change in electrical energy dissipated per period upon the addition of the monomer

$$\Delta E_g = E_g(F_m = 0) - E_g(F_m) \qquad (2)$$

is shown in Figure 3.

The electrical energy dissipated in the DBD per period decreases almost linearly from 1.6 mJ in pure argon to about 1.0 mJ at $F_m = 2$ sccm and remains nearly constant at higher monomer flows. The "plateau" found for E_g and ΔE_g at larger monomer flows has not only been observed for HMDSO, but similarly also for several other plasma polymerisation monomers, which were examined initially, namely simple hydrocarbons, including acetylene.[41]

Notice that E_g evaluated according to Equation (1) is almost the same as the total energy input per period

$$E = \int_{t_0}^{t_0+T} I_m(t) V_{ps}(t) dt. \qquad (3)$$

This is just because there is no further power loss in addition to the power loss by the discharge.

As reported previously, measurements of the Si–CH$_3$/Si–O–Si band ratio in the attenuated total reflectance Fourier-transform infra-red spectra of pp-HMDSO films grown under these conditions with $F_m = 0.4, 1.2, 1.5$, and 6.0 sccm showed that there were gradients in the coating composition in the flow direction for small F_m values up to 1.5 sccm ($x = 150$ ppm), owing to monomer consumption in the discharge.[35] However, the coatings were found to be chemically uniform at higher flow rates ($F_m = 6.0$ sccm, $x = 600$ ppm) in the monomer-rich region, corresponding to the "plateau" of ΔE_g in Figure 3.

3 | DESCRIPTION OF THE MODEL

According to the experimental studies, a plane-parallel discharge configuration is considered, where both electrodes are covered by dielectrics with the properties of Macor ($\Delta_M = 3.5$ mm, $\varepsilon_r = 6.0$) and glass ($\Delta_G = 3.0$ mm, $\varepsilon_r = 4.0$), respectively, which are separated by the gap width $d = 2$ mm. In the model calculations, the electrode on the left side is powered by the AC voltage $V_a(t) = V_{ps}(t) - V_m(t)$ derived from measurements, and the electrode to the right is grounded. Figure 4 shows a schematic representation of the discharge geometry used in the modelling studies.

The theoretical description and analysis of the electrical discharge characteristics of the large-area DBD reactor has been performed by means of a
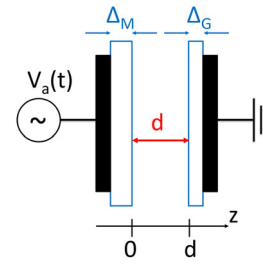
FIGURE 4 Schematic of the spatially one-dimensional discharge geometry with gap d, thicknesses of the dielectric layers Δ_M and Δ_G and applied AC voltage $V_a(t)$

time-dependent, spatially one-dimensional fluid model, where the spatial variation of plasma in the gap takes place along the z-axis. The fluid model includes particle balance equations for the densities n_j of electrons ($j = e$), relevant neutral particles and ions, the electron energy balance equation to determine the mean electron energy u_e, the Poisson equation to calculate the electric potential Φ and electric field E, as well as a balance equation for the surface charge density σ_s to consider the accumulation of charge carriers on the dielectric surfaces at $z_0 = 0$ and $z_0 = d$. A schematic overview of the basic relations and the sequence of their solution is shown in Figure 5. Here e_0, ε_0, and Z_j are the elementary charge, vacuum permittivity, and particle charge number, respectively, and E_D denotes the electric field inside the respective dielectric barrier, $\nu = -1$ at $z_0 = 0$ and $\nu = 1$ at $z_0 = d$.

The particle fluxes Γ_j of heavy particles are determined in the common drift-diffusion approximation, whereas the particle flux Γ_e and energy flux Q_e of electrons are expressed by the improved drift-diffusion approximation introduced by Becker et al.[45,46] Furthermore, S_j denotes gain and loss of particles of kind j in the plasma due to collision processes and radiative transitions, and $\tilde{S}_e$ represents the gain and loss of electron
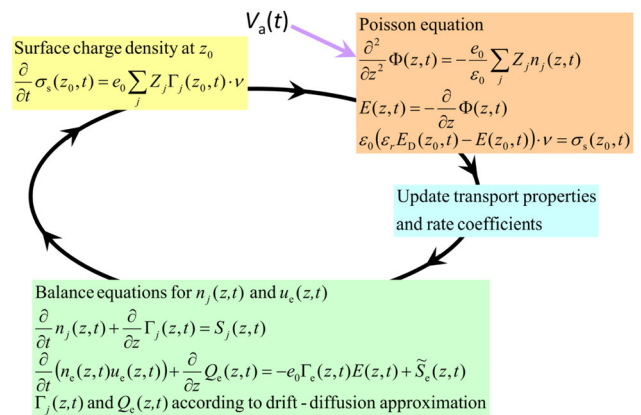

FIGURE 5 Sketch of the time-dependent, spatially one-dimensional fluid model

energy caused by various collision processes involving electrons. A few remarks about the reaction kinetics scheme for Ar–HMDSO mixtures are given above in Section 1. Further details about the reaction kinetics model, basic relations, transport properties and rate coefficients, boundary conditions, and the solution method are reported in Loffhagen et al.[37]

4 | RESULTS AND DISCUSSION

The model calculations were carried out for Ar–HMDSO mixtures at atmospheric pressure and gas temperature of 300 K, with an HMDSO fraction x up to about 1,600 ppm, in accordance with related experimental studies. Note that the spatially one-dimensional model does not include the effect of HMDSO depletion in the flow direction. The HMDSO fractions x corresponding to the monomer input concentration are used for modelling and comparison with experimental data. The implications of this assumption are discussed later in this section.

Figure 6 shows the applied AC voltage $V_a(t)$, as determined from the measurements, and the calculated periodic evolution of the voltage across the gap V_{gap}, the gas current

$$I_g(t) = \underbrace{\frac{A}{d}\int_0^d e_0 \sum_j Z_j \Gamma_j(z,t)\mathrm{d}z}_{I_d(t)} + \underbrace{\frac{A}{d}\int_0^d \varepsilon_0 \frac{\partial E(z,t)}{\partial t}\mathrm{d}z}_{I_{gap}(t)}$$

(4)

and the discharge current I_d for Ar–HMDSO mixtures with x = 20, 100, 600, and 1,570 ppm. These results are compared with the corresponding experimental data derived from the electrical measurements of V_{ps} and V_m and related equivalent circuit analyses discussed in Section 2. Except for the case of x = 20 ppm, there is generally quite a good agreement between the currents I_g and I_d resulting from the model calculations and experimental data. This also concerns the absolute values of the voltages and currents. The experimental peak current densities amount to 0.5 mA/cm^2 at small x and 0.4 mA/cm^2 for $x > 200$ ppm, at a power density of 0.46 W/cm^3, which are characteristic values of glow-like discharges.[47] However, time-dependencies of V_{gap}, I_g, and I_d obtained from experimental data derivation and by numerical modelling show certain differences. The former values are found to be almost independent of the HMDSO admixture for $x > 200$ ppm, whereas the modelling results, performed at a constant number density of HMDSO in Ar, demonstrate a sharper evolution in the gap voltage and currents while also presenting a decrease of the gap voltage at discharge ignition.

To illustrate the impact of the HMDSO addition on the modelling results more clearly, Figure 7 shows applied voltage $V_a(t)$ and the periodic behaviour of the gap voltage $V_{gap}(t)$ and discharge current $I_d(t)$ for x = 150, 470, and 1,440 ppm. The numerical results exhibit one weakly pronounced current peak per half-period, extending over a time span of about 7 μs with a current density around 0.5 mA/cm^2 for small HMDSO admixure,
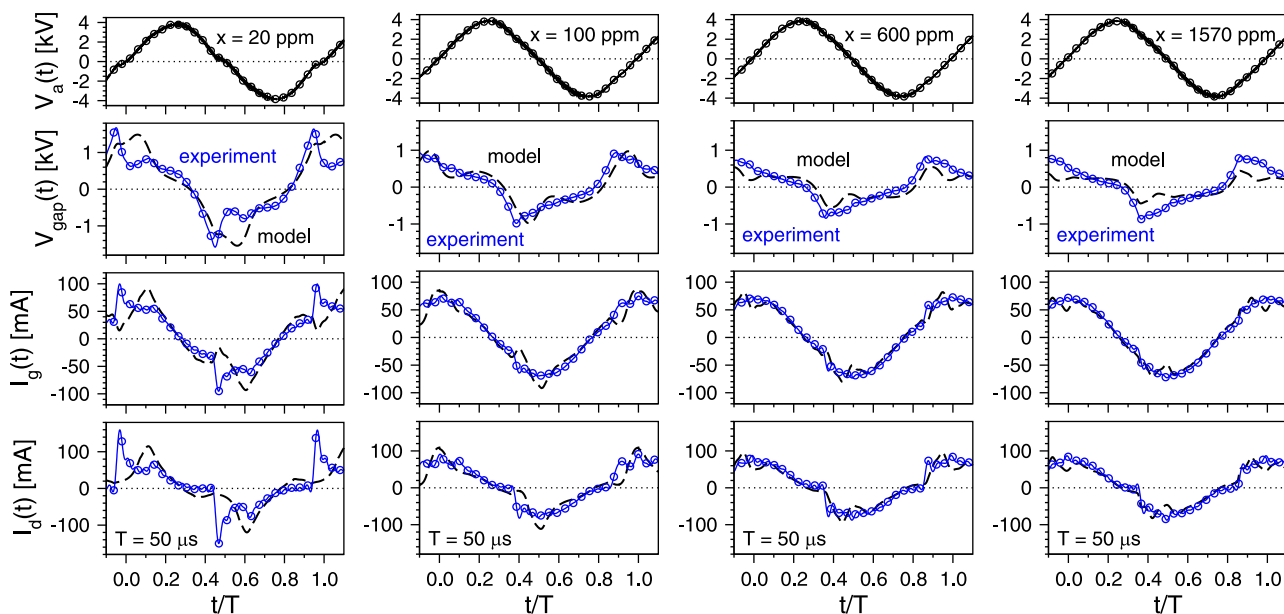

FIGURE 6 Calculated periodic behaviour of the gap voltage V_{gap}, gas current I_g, and discharge current I_d (black dashed lines) at $V_{a,0}$ = 3.9 kV and f = 20 kHz for different HMDSO fractions x in comparison with experimental results (lines with symbols)
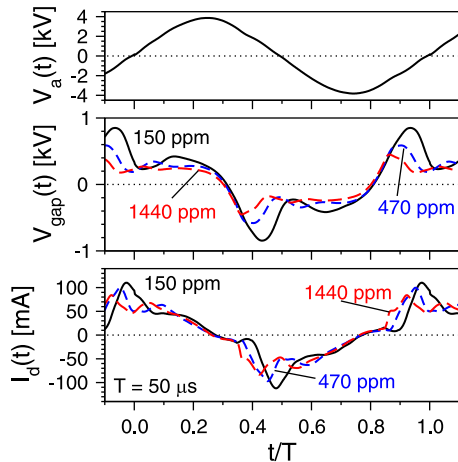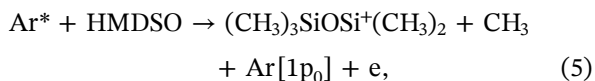
FIGURE 7 Periodic behaviour of the gap voltage V_{gap} and discharge current I_d obtained by numerical modelling for different HMDSO fractions x using the experimental voltage course $V_a(t)$ with $V_{a,0} = 3.9$ kV and $f = 20$ kHz as input
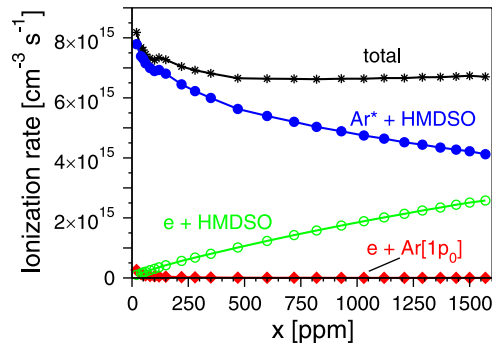

FIGURE 8 Impact of the HMDSO admixture x on the electron production channels obtained by numerical modelling for $V_{a,0} = 3.9$ kV and $f = 20$ kHz

$x < 200$ ppm. At larger values of x, the peak current density decreases to 0.4 mA/cm^2, in accordance with experimental results, and a second weaker current peak of similar duration occurs, which is not found or resolved by the experimental data. In addition, discharge peaks occur earlier during the period because the gap voltage required for ignition decreases with increasing x.[37]

To analyse the ionisation budget for different HMDSO admixtures, Figure 8 represents the total space- and period-averaged ionisation rate as well as individual space- and period-averaged contributions of different reaction channels to the total electron production obtained by numerical modelling for $V_{a,0} = 3.9$ kV, $f = 20$ kHz, and $x \geq 20$ ppm. The total ionisation rate decreases slowly up to about $x = 500$ ppm and remains almost constant then. The Penning ionisation process

$$Ar^* + HMDSO \rightarrow (CH_3)_3SiOSi^+(CH_3)_2 + CH_3$$
$$+ Ar[1p_0] + e, \qquad (5)$$

is the predominant source of electron (e) production over the whole range of HMDSO admixtures. In this reaction, collisions between excited (metastable and resonance) argon atoms (Ar*) and HMDSO molecules lead to the generation of the pentamethyldisiloxanyl ion, a methyl radical, and an argon atom in its ground state $1p_0$ (Paschen notation). Its relative contribution decreases from about 95% at small monomer admixtures to about 60% at $x = 1,570$ ppm. At the same time, the contribution of direct electron impact ionisation of HMDSO according to the process

$$HMDSO + e \rightarrow (CH_3)_3SiOSi^+(CH_3)_2 + CH_3 + 2e \quad (6)$$

increases up to about 40%. Except for the minor contribution of the electron impact ionisation of ground-state argon atoms for small x, the contributions of electron impact ionisation of excited argon atoms and molecules as well as of chemo-ionisation processes in collisions of two excited argon atoms are negligible in the entire x range considered. Thus, they are not displayed in Figure 8.

The corresponding periodic evolution of space-averaged individual ionisation rates for $x = 150$ and $1,440$ ppm is displayed in Figure 9. The features found for period-averaged ionisation rates are also reflected in their temporal variation. Penning ionisation processes (5) dominate the generation of electrons during the entire period, where direct electron impact ionisation of HMDSO (6) becomes increasingly important for larger x. For $x = 150$ ppm, a further, smaller peak in the Penning ionisation rate is found around $t/T = 0.15$ and 0.65. However, this ionisation rate is not sufficient to lead
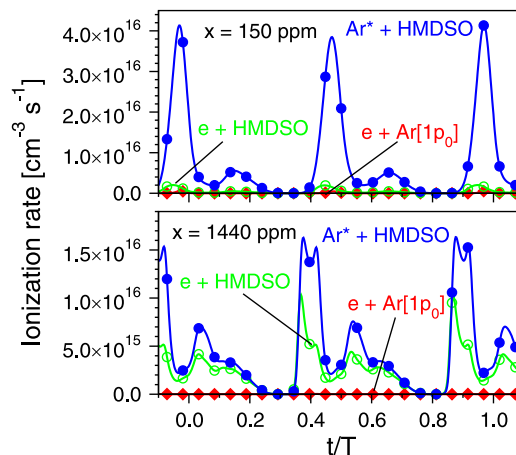

FIGURE 9 Calculated periodic behaviour of individual ionisation rates at $V_{a,0} = 3.9$ kV, $f = 20$ kHz, and $x = 150$ and $1,440$ ppm, respectively

to a second peak in the corresponding discharge current (cf. Figure 7).

Figure 10 displays the spatiotemporal variation of the electron density $n_e(z, t)$ in the logarithmic representation for $V_{a,0} = 3.9$ kV, $f = 20$ kHz, and $x = 150$ and 1,440 ppm, respectively. The powered electrode is on the side of the Macor dielectric and the grounded electrode on that of the glass dielectric (cf. Figure 4). The electron densities show a pronounced alteration in space and time for both cases considered.

Starting around $t/T = -0.2$, the electron density decreases by orders of magnitude for $x = 150$ ppm in the positive half-period when the gap voltage increases (cf. Figure 7). This decrease of $n_e(z, t)$ is most pronounced in the front of the glass dielectric barrier located at $z = 2$ mm (cathode side), because of the drift of electrons towards the anode in the increasing electric field. When the gap voltage approaches its maximum value, an increase of the electron density takes place. The electron avalanche starts in front of the momentary anode located at $z = 0$ and propagates towards the momentary cathode during the discharge pulse. At the current peak, the maximum electron density of about 2.3×10^{11} cm^{-3} occurs in front of the cathode. After the discharge pulse, the bulk plasma region remains almost unchanged in space and time until the gap voltage becomes negative and polarity changes around $t/T = -0.3$. Qualitatively, the same behaviour of $n_e(z, t)$ occurs in the negative half-period.

The spatiotemporal behaviour of $n_e(z, t)$ at $x = 1,440$ ppm exhibits the same features as that for $x = 150$ ppm. Again, a strong drop of the electron density occurs during the change of polarity in front of that dielectric barrier which becomes the cathode, for example, the Macor dielectric after $t/T = 0.3$. The maximum electron density amounts to about 1.4×10^{11} cm^{-3} during the first discharge current peak. At the same time, there are always regions where $n_e(z, t)$ does not fall below 10^{10} cm^{-3} during the entire period. Notice that the space- and period-averaged electron density decreases from about 2.6×10^{10} cm^{-3} at $x = 20$ ppm to about 2.0×10^{10} cm^{-3} at $x = 200$ ppm and remains almost constant for larger x. At the same time, the space- and period-averaged mean energy of the electrons decreases monotonically from about 3.2 eV at small x to about 1.8 eV at $x = 1,600$ ppm.[48]

The differences between experimental and modelling results of the gap voltages and currents shown in Figure 6 are also reflected in the dependence of the corresponding root-mean-square (rms) values of $V_{gap}(t)$, $I_g(t)$, and $I_d(t)$ on x, which are displayed in Figure 11. The experimental values of rms gap voltage decrease by about 350 V up to about $x = 200$ ppm and remain almost constant for larger x, where the rms value of applied voltage is always $V_{a,rms} = 2.6$ kV (not shown in Figure 11). At the same time, the rms values of the currents I_g and I_d derived from measurements are virtually constant for $x \geq 100$ ppm, with values around 49 and 52 mA, respectively. In contrast, modelling results show a monotonic decrease of $V_{gap,rms}$ with increasing x, which is accompanied by a continuous decline of $I_{d,rms}$ at an almost constant calculated $I_{g,rms} = 47$ mA for $x \geq 100$ ppm. Here, deviations of the rms currents obtained by modelling from those derived by experimental equivalent circuit analysis amount to less than 6% for $I_{g,rms}$ and 12% for $I_{d,rms}$.

According to Equation (1), the integral of the product of discharge current $I_d(t)$ and gap voltage $V_{gap}(t)$ over a duration $T = 1/f$ represents the energy dissipated within one period, E_g. Its dependence on x resulting from experimental data derivation and model calculations at $V_{a,0} = 3.9$ kV and $f = 20$ kHz is illustrated in Figure 12. Below $x = 200$ ppm, a substantial decrease of E_g is found in both modelling and experiment. Although the measured value becomes virtually constant for larger values of x, fluid modelling results show a monotonic decrease of E_g with increasing x. This decrease is mainly caused by the impact of Penning ionisation process (5)
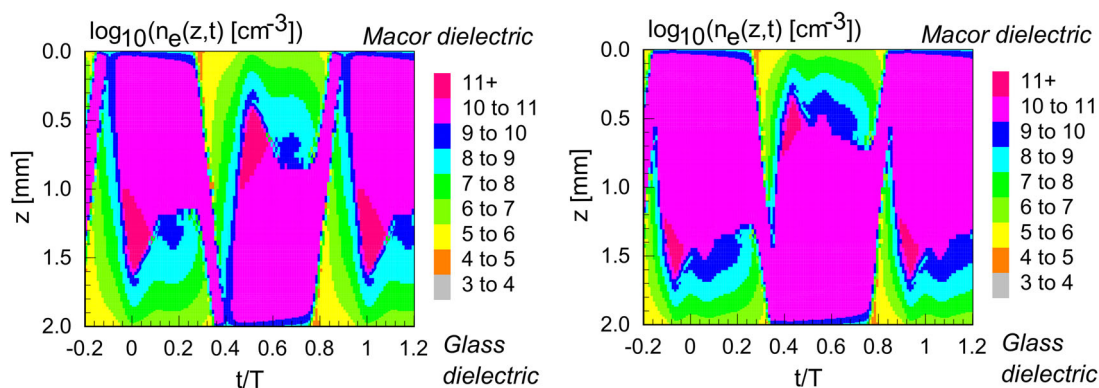

FIGURE 10 Calculated spatiotemporal evolution of the electron density at $V_{a,0} = 3.9$ kV, $f = 20$ kHz, and $x = 150$ ppm (left) and 1,440 ppm (right)
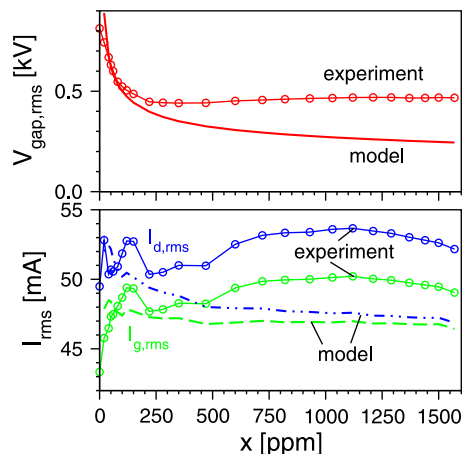
FIGURE 11 Comparison of modelling and experimental results of the root-mean-square (rms) gap voltage $V_{gap,rms}$, gas current $I_{g,rms}$, and discharge current $I_{d,rms}$ for different HMDSO fractions x

and the resulting drop in ignition and gap voltages found by the model calculations. A similar decline in E_g as shown in Figure 12, which becomes progressively smaller for larger x, was also found in experimental and modelling studies reported in the literature.[36,37] However, these investigations were performed in a smaller-sized DBD configuration at power densities between 5 and 10 W/cm^3, where the residence time τ of the plasma was typically 8 ms,[37] that is, much smaller than that for the present large-area DBD reactor experiment operated at power densities around 0.5 W/cm^3, τ being 260 ms.[41] As reported in the related experimental studies,[33,35] for example, there is much reason to believe that the experimental values of E_g are not only highly reproducible, but also precise to roughly 10%. This further emerges from inspection of the experimental data in Figures 11 and 12.

To get information from the modelling studies about the energy absorbed from the DBD plasma by HMDSO molecules, space- and period-integrated energy loss rates due to collisions of HMDSO with electrons, atomic and
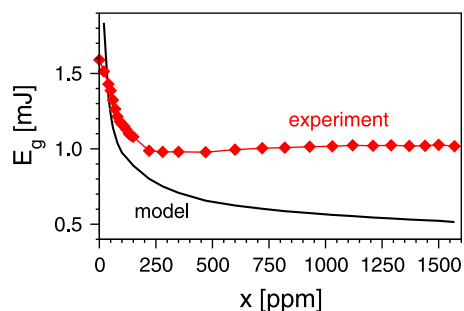
molecular argon ions, and various excited argon species have been determined for the processes detailed in Loffhagen et al.[37] The corresponding total energy loss during a period induced by HMDSO molecules, as well as individual contributions to it caused by collisions of the monomer with electrons, argon ions, excited argon atoms, and molecules are displayed in Figure 13.

The total energy loss per period (black curve) due to HMDSO collisions falls off continuously for $x \geq 20$ ppm, similar to what was found for the case of E_g. The main contribution of energy absorbed by HMDSO molecules results from their collisions with excited argon atoms (Ar*), blue curve. 70% of this process leads to the generation of trimethylsilyl and trimethylsiloxy radical due to the neutral dissociation of HMDSO according to

$$Ar* + HMDSO \rightarrow (CH_3)_3Si + (CH_3)_3SiO + Ar[1p_0],$$
$$(7)$$
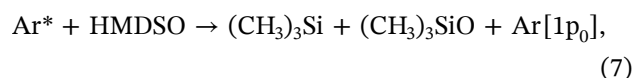
producing the main precursors of the deposited film. The other 30% of the Ar*–HMDSO reaction results from Penning ionisation (5) and leads thus to a gain of electron energy.[37] The relative share of collision processes of Ar* to the total energy loss per period due to HMDSO collisions increases from about 66% to 80% when x rises. Moreover, reactions of excited argon molecules Ar_2^*, namely the triplet excimer in its vibrational ground state,

$$Ar_2^* + HMDSO \rightarrow (CH_3)_3Si + (CH_3)_3SiO + 2Ar[1p_0]$$
$$(8)$$
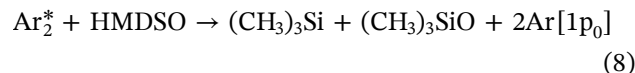
also play an important role for energy loss caused by HMDSO collisions at low x, their relative share decreasing from about 33% to 10% as x increases. This collision process leads to the dissociation of HMDSO to also form neutral trimethylsilyl and trimethylsiloxy film precursors. In addition, collisions of HMDSO molecules with
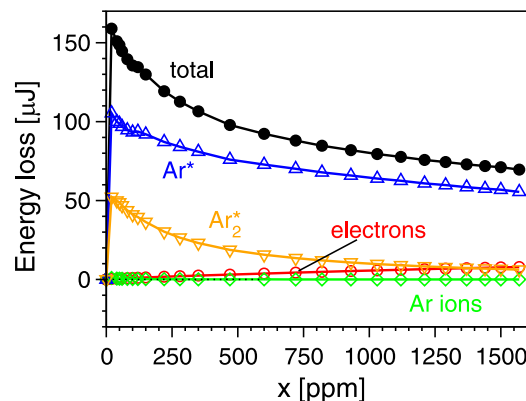

FIGURE 12 Energy E_g dissipated in the discharge per period obtained by numerical modelling and experiment as a function of the HMDSO fraction x

FIGURE 13 Energy loss due to HMDSO collisions as a function of the HMDSO fraction x obtained by numerical modelling for $V_{a,0} = 3.9$ kV and $f = 20$ kHz

electrons gain a relative share of up to about 10% with increasing x, while contributions of HMDSO collisions with atomic and molecular argon ions are almost negligible for the energy loss.

Finally, some comments concerning the almost constant behaviour of measured E_g for larger values of x in Figure 12 should be made. Besides HMDSO, many other added gases in argon have been studied experimentally in a similar manner to that described here.[33,41,49] When adding the hydrocarbons methane (CH$_4$), acetylene (C$_2$H$_2$), ethylene (C$_2$H$_4$), or ethane (C$_2$H$_6$) under similar conditions, a virtual concentration independence of E_g is also found for larger x values.[41] However, CH$_4$ and C$_2$H$_6$ are hardly able to generate electrons due to Penning ionisation processes with Ar*.[50] Thus, this electron-generating process cannot be the sole reason for differences between the measured and calculated E_g values. Furthermore, when adding instead nitrogen (N$_2$) or oxygen (O$_2$) to argon, the resulting measured energy dissipated per period showed a monotonic decrease with increasing admixture of N$_2$ or O$_2$,[41] similar to that obtained here by the model calculations for the Ar–HMDSO mixture.

The sharp bending of measured curves of E_g and ΔE_g towards a virtual admixture independence above HMDSO fractions x of about 200 ppm ($F_m = 2$ sccm) in Figure 3 and 12 suggests that the gas phase becomes "saturated" with HMDSO. One may speculate that the concentration of monomers in the gas phase stays unchanged with a further increase of HMDSO flow due to the formation of nanoparticulate HMDSO plasma-polymers that consume an ever-growing amount of monomer. This effect is not considered in the numerical model, which, as described above, takes into account 21 collision processes of HMDSO with electrons, different excited and ionic argon species, as well as the dissociative recombination of electrons due to collisions with the pentamethyldisiloxanyl ion. However, it thus far neglects the possible formation of nanoparticles or balance equations for other reaction products of the plasma-chemical conversion of monomer during its passage through the plasma.

To roughly estimate the depletion, Δx, of monomer after passage of the 6 cm long flow direction through the experimental reactor during the residence time of 260 ms, the present modelling results have been analysed in more detail. Accordingly, the space- and period-averaged particle loss rates due to collisions of HMDSO with electrons, atomic and molecular argon ions, and various excited argon species have been used to calculate the temporal decay of the particle number density of HMDSO, n_M, according to the rate equation:

$$\frac{d}{dt} n_M(t) = -\nu_M^{loss}(t) n_M(t). \tag{9}$$

Here, ν_M^{loss} denotes the loss frequency of HMDSO due to all the collision processes mentioned above, and it depends indirectly on time t via its dependence on the various particle number densities involved for the different mixtures. The monomer depletion from its inflow into the plasma region at $t = 0$ to its outflow after $\tau = 260$ ms is given by

$$\Delta x = \frac{\left(n_M(t = 0) - n_M(\tau) \right)}{N}, \tag{10}$$

where N is the total gas number density. Δx is shown as a function of the initial HMDSO fraction x in Figure 14. In addition, the corresponding change caused solely by collision processes of HMDSO with excited argon species according to reactions (5), (7), and (8) is displayed, following.[36] Above about $x = 320$ ppm, the monomer depletion decreases monotonically with increasing initial HMDSO fraction, where the progression follows that of the calculated electrical energy dissipated in the discharge per period. This behaviour is predominantly caused by collision processes of HMDSO with excited argon atoms and molecules. For instance, $\Delta x = 230$ ppm of the initial HMDSO fraction of 1,000 ppm is predicted to be consumed, that is 23%, whereas the rest leaves the reactor due to the low loss frequency of HMDSO, ν_M^{loss} (see Equation (9)). Furthermore, for $x \leq 320$ ppm a virtually complete consumption of HMDSO during $\tau = 260$ ms takes place before the gas reaches the reactor outlet. This finding is in good agreement with observations reported by Hegemann et al.[35] for the same experimental conditions as used here. There, it was found that uniform plasma polymer films are deposited from HMDSO only along 3 cm of the reactor length for
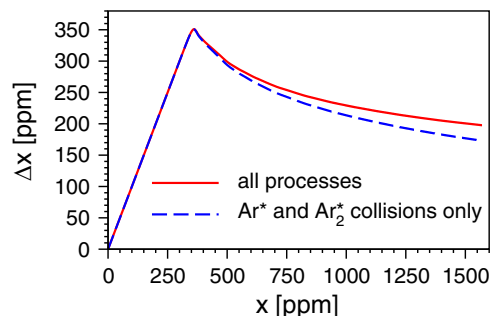

FIGURE 14 Change of monomer fraction Δx after the residence time of 260 ms as a function of the initial HMDSO fraction x derived from the numerical modelling results

$x = 150$ ppm, whereas homogeneous coatings are obtained along the 6 cm reactor length for $x = 600$ ppm. However, the formation of a plateau region for E_g above about $x = 200$ ppm cannot be explained on the basis of this depletion analysis, emphasising once more the hypothesis of nanoparticulate HMDSO polymer formation.

The formation of nanoparticles is a frequently observed phenomenon in atmospheric pressure plasma polymerisation. Depending on their growth rate, electric charge, and the applied frequency, nanoparticles may be incorporated in the growing film or, at higher frequencies, leave the reactor with the gas stream.[47] In fact, formation of nanoparticles in DBDs in Ar with HMDSO and acetylene admixture, respectively, has been reported in the literature.[51] Those discharges ran under conditions similar to the ones used here or in Philipp et al.[34] and Nisol et al.[41] The particles were collected from the gas phase as far as 50 cm downstream from the plasma for 145 ppm HMDSO and 1,000 to 2,000 ppm C_2H_2, respectively, where the residence time of gas in the plasma zone was less than 70 ms.[51] Deposition of films with a milky appearance behind the plasma zone, composed of particles 50 to 100 nm in size, was also reported by Philipp et al. for HMDSO admixtures larger than about 70 ppm,[34] whereas thick powdery deposits were observed to form in DBDs from Ar–C_2H_2 mixtures.[41]

At least by inspecting the deposits, there was no evidence that nanoparticles were actually formed in experiments reported in the present paper. To help clarify the differences between the modelling and experimental results for the E_g shown in Figure 12, it would be very interesting to investigate to what extent the surplus HMDSO leaves the DBD reactor unchanged and as nanoparticulate polymers, respectively, using gas-phase infra-red spectroscopy or mass spectrometry, and a nanoparticle collection method. To diminish the effects of chemical conversion of the monomer, it would also be helpful to study shorter residence times in the reactor. Such studies would also benefit from advanced calculations employing a more elaborate reaction kinetics model to understand the plasma-chemical conversion of monomers in more detail.

5 | SUMMARY

Comparative experimental and fluid modelling studies have been performed to analyse the electrical characteristics of Ar–HMDSO plasmas in a large-area reactor for performing DBD experiments at atmospheric pressure. The temporal evolution of gap voltages and discharge currents was determined experimentally using measured voltage and current signals and applying a related equivalent circuit analysis for HMDSO admixtures, x, up to about 1,600 ppm. Numerical modelling was carried out for the same range of HMDSO admixture by means of a time-dependent, spatially one-dimensional fluid model, which includes an established reaction kinetics scheme for argon, as well as 22 reactions related to HMDSO, and uses the measured applied AC voltage as input.

The gap voltages and discharge currents obtained by experiment and modelling agree reasonably well in general, where the Penning ionisation processes of excited argon atoms with HMDSO molecules were determined by the model calculations to play a predominant role for the ionisation budget. The comparison of the related measured and calculated electrical energy dissipated in the plasma per period E_g showed qualitative agreement for small admixtures up to about $x = 200$ ppm, but increasing differences for larger x, where the measured E_g is virtually constant and the modelling results continue to decrease monotonically. Discussion of different options to explain these deviations in E_g clearly demonstrates the need for future experimental and modelling studies for clarification.

ORCID

Detlef Loffhagen http://orcid.org/0000-0002-3798-0773

Markus M. Becker http://orcid.org/0000-0001-9324-3236

Dirk Hegemann http://orcid.org/0000-0003-4226-9326

Bernard Nisol http://orcid.org/0000-0001-7785-6307

Claus-Peter Klages http://orcid.org/0000-0001-5678-5845

REFERENCES

[1] R. Abbas, A. Schedemann, C. Ihmels, S. Enders, J. Gmehling, *Ind. Eng. Chem. Res.* **2011**, *50*, 9748.

[2] *Nonthermal Plasma Chemistry and Physics* (Eds: J. Meichsner, M. Schmidt, R. Schneider, H.-J. Wagner), CRC Press, Boca Raton, FL **2013**.

[3] M. J. Vasile, G. Smolinsky, *J. Electrochem. Soc.* **1972**, *119*, 451.

[4] Y. Segui, B. Ai, *J. Appl. Polym. Sci.* **1976**, *20*, 1611.

[5] W. Möller, M. Schmidt, *Beitr. Plasmaphys.* **1977**, *17*, 121.

[6] A. M. Wróbel, M. R. Wertheimer, J. Dib, H. P. Schreiber, *J. Macromol. Sci. A* **1980**, *14*, 321.

[7] A. M. Wróbel, J. E. Klemberg, M. R. Wertheimer, H. P. Schreiber, *J. Macromol. Sci. A* **1981**, *15*, 197.

[8] W. Möller, M. Schmidt, R. Seefeldt, R. Wilberg, *Beitr. Plasmaphys.* **1984**, *24*, 629.

[9] K.-D. Schulz, M. Schmidt, *Acta Polym.* **1984**, *35*, 257.

[10] S. Sahli, Y. Segui, S. HadjMoussa, M. A. Djouadi, *Thin Solid Films* **1992**, *217*, 17.

[11] S. Sahli, Y. Segui, S. Ramdani, Z. Takkouk, *Thin Solid Films* **1994**, *250*, 206.

[12] A. M. Sarmadi, T. H. Ying, F. Denes, *Eur. Polym. J.* **1995**, *31*, 847.

[13] M. R. Alexander, F. R. Jones, R. D. Short, *J. Phys. Chem. B* **1997**, *101*, 3614.

[14] M. R. Alexander, F. R. Jones, R. D. Short, *Plasmas Polym.* **1997**, *2*, 277.

[15] F. Benítez, E. Martínez, J. Esteve, *Thin Solid Films* **2000**, *377-378*, 109.

[16] C. Vautrin-Ul, C. Boisse-Laporte, N. Benissad, A. Chausse, P. Leprince, R. Messina, *Prog. Org. Coat.* **2000**, *38*, 9.

[17] D. Hegemann, H. Brunner, C. Oehr, *Surf. Coat. Technol.* **2001**, *142-144*, 849.

[18] S. Zanini, C. Riccardi, M. Orlandi, P. Esena, M. Tontini, M. Milani, V. Cassio, *Surf. Coat. Technol.* **2005**, *200*, 953.

[19] A. Michelmore, P. M. Bryant, D. A. Steele, K. Vasilev, J. W. Bradley, R. D. Short, *Langmuir* **2011**, *27*, 11943.

[20] J. Schäfer, R. Foest, A. Quade, A. Ohl, K.-D. Weltmann, *J. Phys. D: Appl. Phys.* **2008**, *41*, 194010.

[21] U. Lommatzsch, J. Ihde, *Plasma Process. Polym.* **2009**, *6*, 642.

[22] M. Wolter, S. Bornholdt, M. Häckel, H. Kersten, *J. Achievem. Mater. Manuf. Eng.* **2009**, *37*, 730.

[23] J. Schäfer, R. Foest, F. Sigeneger, D. Loffhagen, K.-D. Weltmann, U. Martens, R. Hippler, *Contrib. Plasma Phys.* **2012**, *52*, 872.

[24] J. Benedikt, D. Ellerweg, S. Schneider, K. Rügner, R. Reuter, H. Kersten, T. Benter, *J. Phys. D: Appl. Phys.* **2013**, *46*, 464017.

[25] J. Schäfer, F. Sigeneger, R. Foest, D. Loffhagen, K.-D. Weltmann, *Eur. Phys. J. D* **2018**, *72*, 90.

[26] R. Foest, F. Adler, F. Sigeneger, M. Schmidt, *Surf. Coat. Technol.* **2003**, *163-164*, 323.

[27] D. Trunec, Z. Navrátil, P. Sťahel, L. Zajíčková, V. Buršíková, J. Čěch, *J. Phys. D: Appl. Phys.* **2004**, *37*, 2112.

[28] M. Hähnel, V. Brüser, H. Kersten, *Plasma Process. Polym.* **2007**, *4*, 629.

[29] R. Morent, N. de Geyter, S. van Vlierberghe, P. Dubruel, C. Leys, E. Schacht, *Surf. Coat. Technol.* **2009**, *203*, 1366.

[30] R. Morent, N. de Geyter, S. van Vlierberghe, P. Dubruel, C. Leys, L. Gengembre, E. Schacht, E. Payen, *Prog. Org. Coat.* **2009**, *64*, 304.

[31] R. Morent, N. de Geyter, T. Jacobs, S. van Vlierberghe, P. Dubruel, C. Leys, E. Schacht, *Plasma Process. Polym.* **2009**, *6*, S537.

[32] L. Zhou, G.-H. Lv, H. Pang, G.-P. Zhang, S.-Z. Yang, *Surf. Coat. Technol.* **2012**, *206*, 2552.

[33] B. Nisol, S. Watson, S. Lerouge, M. R. Wertheimer, *Plasma Process. Polym.* **2016**, *13*, 557.

[34] J. Philipp, A. K. Czerny, C.-P. Klages, *Plasma Process. Polym.* **2016**, *13*, 509.

[35] D. Hegemann, B. Nisol, S. Watson, M. R. Wertheimer, *Plasma Chem. Plasma Process.* **2017**, *37*, 257.

[36] C.-P. Klages, A. K. Czerny, J. Philipp, M. M. Becker, D. Loffhagen, *Plasma Process. Polym.* **2017**, *14*, 1700081.

[37] D. Loffhagen, M. M. Becker, A. K. Czerny, J. Philipp, C.-P. Klages, *Contrib. Plasma Phys.* **2018**, *58*, 337.

[38] M. M. Becker, T. Hoder, R. Brandenburg, D. Loffhagen, *J. Phys. D: Appl. Phys.* **2013**, *46*, 355203.

[39] P. Raynaud, B. Despax, Y. Segui, H. Caquineau, *Plasma Process. Polym.* **2005**, *2*, 45.

[40] K. Rügner, R. Reuter, D. Ellerweg, *Plasma Process. Polym.* **2013**, *10*, 1061.

[41] B. Nisol, H. Gagnon, S. Lerouge, M. R. Wertheimer, *Plasma Process. Polym.* **2016**, *13*, 366.

[42] M. Archambault-Caron, H. Gagnon, B. Nisol, K. Piyakis, M. R. Wertheimer, *Plasma Sources Sci. Technol.* **2015**, *24*, 045004.

[43] B. Nisol, S. Watson, H. Gagnon, M. R. Wertheimer, *Plasma Process. Polym.* **2018**, *15*, 1800119.

[44] S. Watson, B. Nisol, H. Gagnon, M. Archambault-Caron, F. Sirois, M. R. Wertheimer, *IEEE Trans. Plasma Sci.* **2019**, *47*, 2680.

[45] M. M. Becker, D. Loffhagen, *AIP Adv.* **2013**, *3*, 012108.

[46] M. M. Becker, H. Kählert, A. Sun, M. Bonitz, D. Loffhagen, *Plasma Sources Sci. Technol.* **2017**, *26*, 044001.

[47] F. Massines, C. Sarra-Bournet, F. Fanelli, N. Naudé, N. Gherardi, *Plasma Process. Polym.* **2012**, *9*, 1041.

[48] D. Loffhagen, M. M. Becker, Plasma parameters in an Ar–HMDSO DBD at atmospheric pressure for plasma-polymerization experiments, **2019**, last accessed 6 November 2019, https://doi.org/10.34711/inptdat.106

[49] B. Nisol, S. Watson, A. Meunier, D. Juncker, S. Lerouge, M. R. Wertheimer, *Plasma Process. Polym.* **2018**, *15*, 1700132.

[50] J. Balamuta, M. F. Golde, Y. Ho, *J. Chem. Phys.* **1983**, *79*, 2822.

[51] V. Vons, Y. Creyghton, A. Schmidt-Ott, *J. Nanopart. Res.* **2006**, *8*, 721.